

## Key Points:

- The sea surface height (SSH) variability in the 30–120 km wavelength band was derived from altimetry along-track SSH variance spectra
- High SSH variability in the 30–120 km wavelength band was found in the intratropics of all oceans and in five regions along the Antarctic Circumpolar Current
- The average spectral slope in the 30–120 km wavelength band in the intratropics was about  $-2.14$ – $-1.56$ , consistent with Garrett-Munk model

## Correspondence to:


S. Chen,  
[schen@soest.hawaii.edu](mailto:schen@soest.hawaii.edu)

## Citation:

Chen, S., & Qiu, B. (2021). Sea surface height variability in the 30–120 km wavelength band from altimetry along-track observations. *Journal of Geophysical Research: Oceans*, 126, e2021JC017284. <https://doi.org/10.1029/2021JC017284>

Received 13 FEB 2021  
Accepted 26 MAR 2021

# Sea Surface Height Variability in the 30–120 km Wavelength Band From Altimetry Along-Track Observations

Shuiming Chen<sup>1</sup>  and Bo Qiu<sup>1</sup>

<sup>1</sup>Department of Oceanography, University of Hawaii at Manoa, Honolulu, HI, USA

**Abstract** Reprocessed altimetry along-track sea surface height (SSH) observations from multiple missions are analyzed for the SSH variability in the 30–120 km wavelength band. This band of variability is missing in the widely used global multi-mission mapped SSH data set, known as the Archiving, Validation and Interpretation of Satellite Oceanographic Data SSH product. The SSH variability is derived from along-track SSH variance spectra after subtracting noise floors, and its global spatial patterns are consistent among the missions and the output of a high-resolution ocean general circulation model simulation. High SSH variability in the 30–120 km wavelength band is found in the intratropics of all ocean basins (25°S–25°N), the western boundary current outflow regions, and in five regions along the Antarctic Circumpolar Current: Agulhas Retroflexion zone, Kerguelen Plateau, Macquarie Ridge, Pacific Antarctic Ridge, and Drake Passage. The average slope of the along-track SSH spectra in the 30–120 km wavelength band in the intratropics falls between  $-2.14$  and  $-1.56$ , consistent with the Garrett-Munk spectral slope. The spatial patterns of the SSH variability could be used as a metric to evaluate high-resolution numerical models and to shed light on what to expect from future high-resolution altimetry missions.

**Plain Language Summary** Sea surface height (SSH) varies on different spatial scales and plays different dynamical roles. SSH associated with strong surface gravity waves on the scale of several meters affects navigation. Large swells of a few hundreds of meters generate large surfing waves. Eddies of tens to hundreds of kilometers in size pump cold and nutrient-rich water to near-surface euphotic zones. Large scale ocean gyres collect plastic garbage over thousands of kilometers at their centers. In this study, we focus on the global SSH variability with the scale of 30–120 km by analyzing along-track SSH data from satellite altimetry missions of the past two decades that have a nominal spatial resolution of  $\sim 7$  km. To derive the unbiased SSH variability, we carefully remove the measurement noise. We have obtained consistent global patterns of the SSH variability in the 30–120 km wavelength band and have explored its connection to the larger mesoscale SSH variability in the 120–500 km wavelength band, its spectral characteristics, and its seasonal modulation.

## 1. Introduction

Satellite altimetry sea surface height (SSH) observations have greatly advanced studies on ocean dynamics from global to mesoscale scales (see Fu et al., 2019 for a comprehensive review). The global multi-mission mapped SSH with a uniform longitude/latitude grid, known as the Archiving, Validation and Interpretation of Satellite Oceanographic Data (AVISO) product, is the most used SSH product. Due to the wide spacing between satellite ground tracks that requires optimal interpolation in time and space during the gridding process (Ducet et al., 2000), its spatial spectral resolution is  $\sim 200$  km in midlatitudes (Ballarotta et al., 2019; Chelton et al., 2011). The along-track SSH data, on the other hand, provides us with opportunities to explore the SSH variability with the spatial scales shorter than  $\sim 200$  km. Recently great effort has been put into processing and reprocessing all nadir altimetry missions to increase the quality of data through reducing errors and improving homogeneity, example with the continuously improving processing algorithms and calibration datasets, such as tide models, applied to all past and present missions (Morrow et al., 2018). In this study, we use the reprocessed along-track data to examine the SSH variability in the 30–120 km wavelength band. This wavelength band is selected because it includes the SSH signals that are missing in

the AVISO gridded product but excludes the shorter SSH signals that are dictated by measurement noises (Dibarboure et al., 2014).

The 30–120 km SSH signals analyzed in this study are defined as square root of the variance, which is obtained by integrating the along-track SSH spectrum in the 30–120 km wavelength band, and are henceforth referred to as *rms SSH*. The advantage of using spectrum instead of band-pass filtered along-track SSH data is that the noise floors are evident at short wavelengths in all along-track SSH spectra and can be subtracted out as done in previous studies on along-track SSH spectral slopes (Dufau et al., 2016; Vergara et al., 2019; Xu & Fu, 2012).

Previous studies by Ballarotta et al. (2019), Dufau et al. (2016), Vergara et al. (2019), and Xu and Fu (2012) made use of the along-track SSH spectral slopes at around 70–250 km to illustrate mesoscale dynamics, without exploring the *rms SSH* signals as this study aims to do. The reason could be that the global distribution of the *rms SSH* at the mesoscales has been established well before those studies (Fu et al., 2019). In comparison, the *rms SSH* in the 30–120 km wavelength band has not been previously examined. In addition to the *rms SSH* signals, we will also in this study quantify the spectral slopes in the 30–120 km wavelength band in the intratropics (25°S–25°N) to complement the afore-mentioned studies.

The objectives of our present study are to present the global distribution of the *rms SSH* values in the 30–120 km wavelength band, including their connection to the larger mesoscale SSH variability (in the 120–500 km wavelength band), their spectral characteristics, and their seasonal modulations. The SSH variability in the 30–120 km band can be dominated by either balanced or unbalanced upper ocean motions, depending on geographic locations and dynamic regimes (Chereskin et al., 2019; Qiu et al., 2017, 2018; Rocha, Chereskin, et al., 2016; Torres et al., 2018). Although no analysis is made to disentangle the SSH signals associated with the balanced versus unbalanced motions, we do include the corresponding results from the global 1/48° MITgcm simulation to provide a context for the altimetry-based results. Our study is relevant to two research communities. The results can be used as a metric to validate and quantify the fidelity of high-resolution global ocean general circulation models, and they will also be of interest to the forthcoming Surface Water and Ocean Topography (SWOT) mission that is expected to capture the 2-dimensional SSH signals down to 15 km wavelengths (Morrow et al., 2019; Wang et al., 2019).

## 2. Datasets and Methods

Along-track SSH datasets from three altimetry missions are used: the first is from the Ku-band Jason 1/2/3 missions (hereafter J123 for brevity), the second from the Ka-band Saral/AltiKa mission (Saral), and the third from the Ku-band Sentinel-3A mission in the Synthetic Aperture Radar mode (S3A).

The 1 Hz along-track SSH data of J123 (01/2002–09/2020) and of Saral (03/2013 to 08/2020) are from the Level-2+ (L2P) products in non-time-critical delay provided by AVISO+ (<https://www.aviso.altimetry.fr/>). As L2P products, all instrumental, environmental, and geophysical corrections have been applied, and the 20-years mean SSH over 1993–2012, MSS-CNES-CLS15, has been removed. The along-track SSH data are given at their original positions, and the average distances between data points are 5.9 km for J123 and 7.0 km for Saral. Minor satellite orbit variations often lead data points to drift a few kilometers between cycles. However, such orbital deviations have little impact on the averaged wavenumber spectrum results of our interest because the spectra are evaluated independently for individual cycles and ground-track segments.

The 20 Hz S3A along-track SSH product in the Low-Resolution with Range Migration Correction (LR-RMC) mode from July 2016 to August 2018 is also provided by AVISO+. All standard corrections have been applied and the mean SSH of MSS-CNES-CLS15 has been removed. The average distance between the 20 Hz S3A data points is 0.34 km. The LR-RMC method is one of the most promising altimeter data processing solutions to deal with the inhomogeneous sea state issue while keeping the high precision of delay/Doppler measurements (Boy et al., 2017; Moreau et al., 2021).

To provide a context for the results based on altimeter data, we also analyze the output of the ocean general circulation model, MITgcm (Marshall et al., 1997), that has a 1/48° horizontal resolution, 90 vertical levels, and was forced by 6-hourly ERA-Interim atmospheric reanalysis (Menemenlis et al., 2008). Because this

high-resolution global simulation was additionally forced by a synthetic surface pressure field consisting of 16 most dominant tidal constituents, the modeled internal tides and internal gravity wave continuum compared favorably with observations (Arbic et al., 2018). The hourly model SSH from 11/2011 to 10/2012, without its yearly mean, is interpolated onto the 1 Hz S3A nominal along-track grid, with an average distance of 6.7 km.

Ensemble mean along-track SSH wavenumber spectra are obtained for each 1000 km zonal  $\times$  500 km meridional region centered at every 5° longitude and every 2° latitude in global ocean. The regions of our selection are smaller than those in previous studies: 10°  $\times$  10° regions were used by Xu and Fu (2012) and 15°  $\times$  15° regions by Vergara et al. (2019). Notice that our study focuses on the 30–120 km wavelength band while previous studies were interested in the mesoscale wavelength band of about 70–250 km. The SSH wavenumber spectra are estimated for each ground track of J123, Saral, and S3A that is at least 500 km long; only the central 500 km portion of the data is used in actual spectral calculations. The mean wavenumber spectrum for each region and mission is obtained by averaging over all available ground tracks and over the mission duration and examples of the derived SSH variance spectra are shown in Figures 1a–1f. The double periodic technique is applied in the spectral estimate for its better wavenumber resolution. Mean SSH variance spectra similar to Figures 1a–1f are obtained by detrending the along-track SSH data and using a 500 km Hanning window (not shown).

To obtain stable spectral estimates toward the Nyquist wavelength, a “no missing data criterion” is implemented: any segments that contain one or more points of missing data are excluded. Interpolation to fill missing data can mask the noise floors at short wavelengths (Dufau et al., 2016). Segments are also excluded if they have outliers due to rough sea state, such as large winds, swells, and rain cells. Overall 10%–30% of the segments are excluded in our spectral estimates. We could clearly identify the spectral noise floors by the flattening of the spectra toward the Nyquist wavelengths for all missions. In Figures 1a–1f the noise floors are indicated by the horizontal black, blue, and red dashed lines for J123, Saral, and S3A, respectively. They are estimated from the least squares fitting of a horizontal line in the 30 km to the Nyquist wavelength range, and are then subtracted from the spectra at all wavelengths.

Our noise removal method is applicable when the noise associated with the measurement errors is white and when it flattens the spectrum (see Figures 1a–1f). We have chosen not to analyze the 1 Hz S3A L2P product since it has a red noise characteristic as pointed out by Vergara et al. (2019). The noise in the along-track 1 Hz SSH measurements in J123 and Saral missions is likely resulted from the spectral hump, may not be white, and can bias our analysis (Dibarboure et al., 2014). Since the 2-years LR-RMC 20 Hz S3A along-track SSH data is free of spectral hump and the MITgcm output involves no measurement noise, comparable features among all missions and MITgcm are deemed realistic.

It is worth emphasizing that by removing the noise floor in the wavenumber space, we are able to estimate the rms amplitude of the de-noised SSH signals in the wavelength range where their spectral variance is above the noise floor. Lack of noise's phase information, however, prevents us from knowing the phases of the de-noised SSH signals. As shown in Figures 1a–1f, the spectral levels in the 30–120 km wavelength band are above the noise floors in all altimetry missions. As long as the white noise is well represented by the noise floor and is lower than the spectrum levels at 30–120 km wavelengths, the variance, then the rms SSH, in the 30–120 km wavelength band can be estimated as the difference between the spectrum levels and the noise floor. In this sense, the SSH signal at 30–120 km wavelengths is called partially resolved. Conceivably, the more elevated the spectral levels above the noise floor, the more reliable the variance and rms SSH estimations. The noise floors in J123 and Saral are much higher than that in S3A. This likely explains that the rms SSH values in J123 and Saral are underestimated by about 25% when compared to those in S3A.

### 3. SSH Variability in the 30–120 km Wavelength Band

Figures 1a–1f show that the SSH variance spectra along 160°W in the 120–500 km wavelength band are, by and large, the same for all altimetry missions and that no significant changes are detected with or without the noise floor removal (thick vs. thin lines). Similar spectral results are also obtained from the MITgcm simulation (green lines). On the contrary, the SSH variance spectra in the 30–120 km wavelength band are significantly impacted by the removal of noise floors. After subtracting the noise floors, the SSH spectra

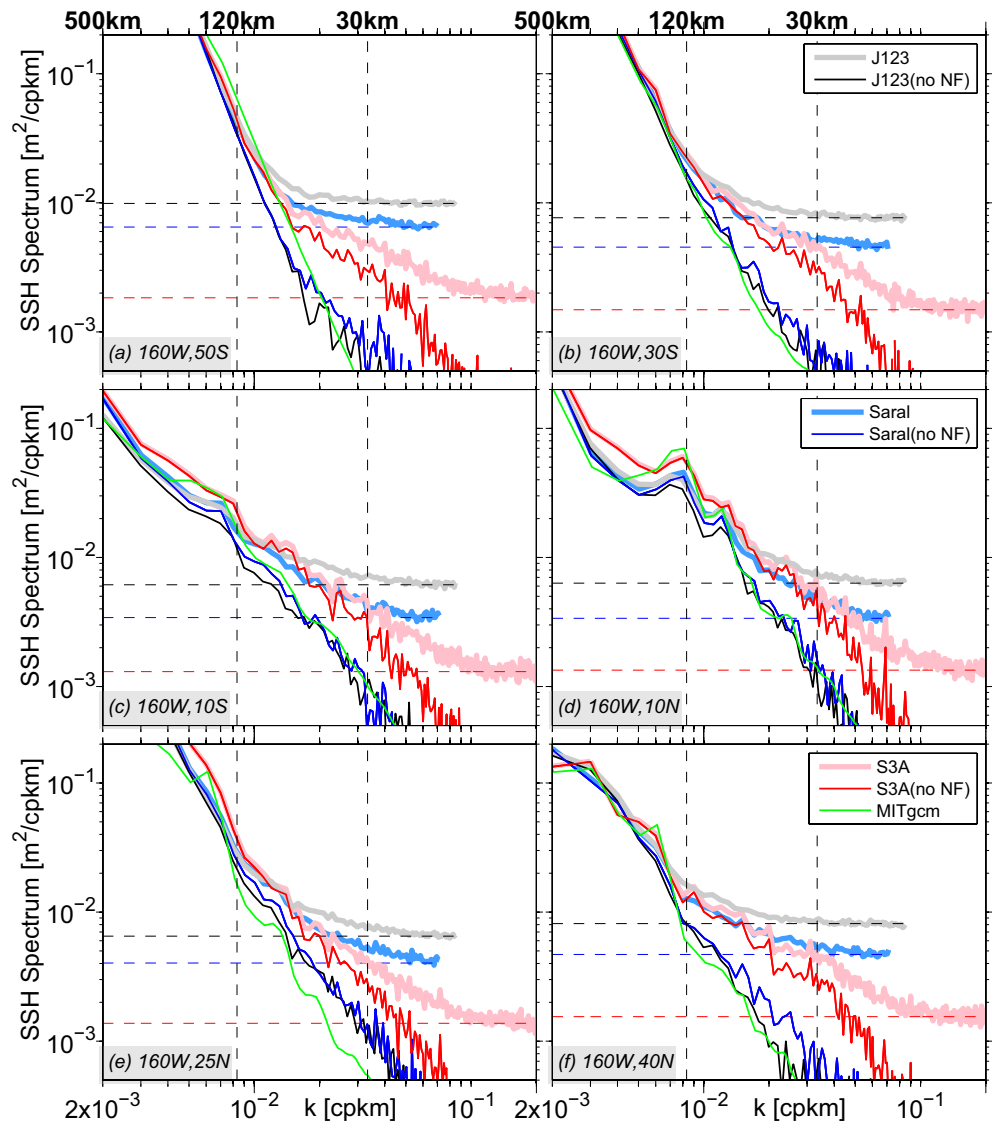


**Figure 1.** (a–f) SSH spectra from along-track 500 km segments for J123 (gray and black lines, before and after subtracting the noise floor (NF) that is indicated by the black horizontal dashed line), for Saral (blueish lines), for S3A (reddish lines), and for MITgcm (green line). The Nyquist wavelengths are 11.8, 14.0, 0.68 km (beyond the abscissa range), and 13.4 km for J123, Saral, S3A, and MITgcm, respectively. The along-track 500 km segments fall into the  $1000 \times 500$  km regions centered at the longitude and latitude shown in the lower left corner.

in the 30–120 km wavelength band for J123 and Saral trend similarly along that for MITgcm, but the S3A spectra remain at high power level almost everywhere in the 30–120 km band.

The rms SSH values along  $160^\circ\text{W}$  in the 120–500 km wavelength band (Figure 2a) are similar across all missions and MITgcm while those in the 30–120 km wavelength band (Figure 2b) are similar among J123, Saral, and MITgcm but not S3A. Local maxima along  $50^\circ\text{S}$ – $60^\circ\text{S}$ ,  $20^\circ\text{N}$ – $30^\circ\text{N}$ , and  $50^\circ\text{N}$  are seen in both 120–500 km and 30–120 km bands. Physically, these maxima correspond to enhanced eddy variability associated with the Antarctic Circumpolar Current (ACC), the North Pacific Subtropical Countercurrent (STCC), and the Alaskan Stream, respectively. Additional maxima appear near  $20^\circ\text{S}$ – $30^\circ\text{S}$  in the 120–500 km band corresponding to the South Pacific STCC (Qiu & Chen, 2004) and near  $10^\circ\text{N}$  in the 30–120 km band in connection to the North Equatorial Countercurrent. In Figure 2b, the average rms SSH values of Saral, J123, and MITgcm are 76%, 70%, and 73% of that of S3A, respectively.

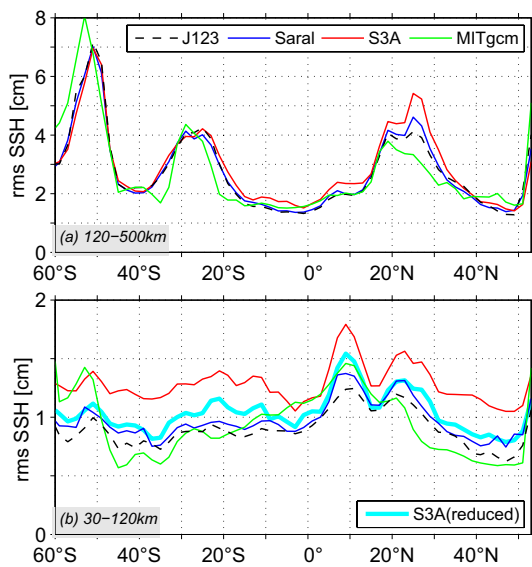


**Figure 2.** (a) rms SSH values in the 120–500 km wavelength band from the spectra associated with the  $1000 \times 500$  km regions centered at  $160^\circ\text{W}$  and latitudes in the abscissa, several of which are shown in Figures 1a–1f. (b) Same as panel (a), except in the 30–120 km wavelength band. The additional cyan line for S3A (reduced) relates to Figure 8 that is explained in the discussion section.

The global rms SSH distributions in the 120–500 km wavelength band for S3A and MITgcm (Figures 3a and 3b, those for J123 and Saral are not shown but essentially the same) are contrasted to those in the 30–120 km wavelength band for S3A, Saral, J123, and MITgcm (Figures 3c–3f). The global averages from Figures 3a–3f are 3.9, 4.2, 1.4, 1.1, 1.0, and 1.2 cm, respectively. All hotspots of the rms SSH values in the 120–500 km wavelength band, example in the regions of ACC, western boundary currents (WBCs), and Leeuwin Current, have elevated rms SSH values in the 30–120 km wavelength band. These SSH variabilities in both 120–500 km and 30–120 km bands are thus likely governed by the same balanced instability dynamics, with the 30–120 km SSH signals representing the shorter portions of the instability-induced mesoscale turbulence. The transition scales from balanced to unbalanced motions at those hotspots have been observed to be in the order of tens of kilometers (Callies & Ferrari, 2013; Qiu et al., 2017; Rocha, Chereskin, et al., 2016). This implies that the same balanced dynamics dominates the motions at the wavelengths longer than tens of kilometers, which include both 120–500 km and 30–120 km bands.

The rms SSH variability in the 30–120 km wavelength band is broadly enhanced in the intratropics of all ocean basins ( $25^\circ\text{S}$ – $25^\circ\text{N}$ ), with local maxima appearing to be linked to the Intertropical Convergence Zones (ITCZs) along  $\sim 10^\circ\text{N}$  in the North Pacific and around equator in the Atlantic Ocean, the South Pacific Convergence Zone along  $\sim 10^\circ\text{S}$  east of Papua New Guinea, and the Indian Ocean ITCZ along  $\sim 10^\circ\text{S}$  east of African. These local maxima are also approximately co-located with the

North Equatorial Countercurrents in the Pacific and Atlantic Oceans, and the South Equatorial Countercurrents in the South Pacific and South Indian Oceans. The rms SSH values in Figures 3c–3f are enhanced in the western basins of the Pacific Ocean; similar but less prominent patterns can be recognized in the rms SSH values in the 120–500 km wavelength band in Figures 3a and 3b. Additionally, five concentrated regions of high rms SSH values in the 30–120 km wavelength band along ACC are identifiable in all altimetry missions and MITgcm: Agulhas Retroflexion zone, Kerguelen Plateau, Macquarie Ridge, Pacific Antarctic Ridge, and Drake Passage.

The ratio between the rms SSH values in the 30–120 km and 120–500 km wavelength bands can be as large as 0.8 in the intratropics (Figures 4a–4d). Across all altimetry missions and MITgcm, the Atlantic intratropics have the largest ratio in part due to the lower rms SSH values in the 120–500 km wavelength band. Outside of the tropics, two local maxima are found in the northeast ( $30^\circ\text{N}$ – $50^\circ\text{N}$ ) and southeast ( $30^\circ\text{S}$ – $50^\circ\text{S}$ ) Pacific Ocean, and they appear more prominent in S3A than others.

### 3.1. Spectral Slopes in the 30–120 km Wavelength Band in the Intratropics

Figures 5a–5d show the intratropical distribution of the spectral slopes in the 30–120 km wavelength band. Examples of the spectra from which the slopes were derived can be seen in Figures 1c–1e. To ensure the spectral slope estimate over a wavelength range is sensible, one single dynamics must dominate that wavelength band. This was emphasized in the recent study by Vergara et al. (2019) who varied wavelength range to quantify the mesoscale spectral slopes. Based on the MITgcm simulation, Qiu et al. (2018) showed that the transition scales from balanced to unbalanced motions in the intratropics are larger than 120 km (their Figure 12). In other words, the spectral slopes in Figures 5a–5d are reasonably representative of the unbalanced motions such as internal tides and internal gravity wave continuum.

The average spectral slopes in the intratropics are  $-2.00$ ,  $-2.01$ , and  $-2.14$  for Saral, J123, and MITgcm, respectively (Figures 5b–5d), and are consistent with the predicted  $-2$  slope for internal gravity waves by the Garrett-Munk (GM) model (Munk, 1981). Noticeably the average slope of  $-1.56$  for S3A in Figure 5a tends to be flatter, a result also visually discernible in Figures 1c–1e. Spatial patterns common to all missions and MITgcm include flatter slopes in the eastern basins of all oceans, most prominently the Atlantic Ocean, and



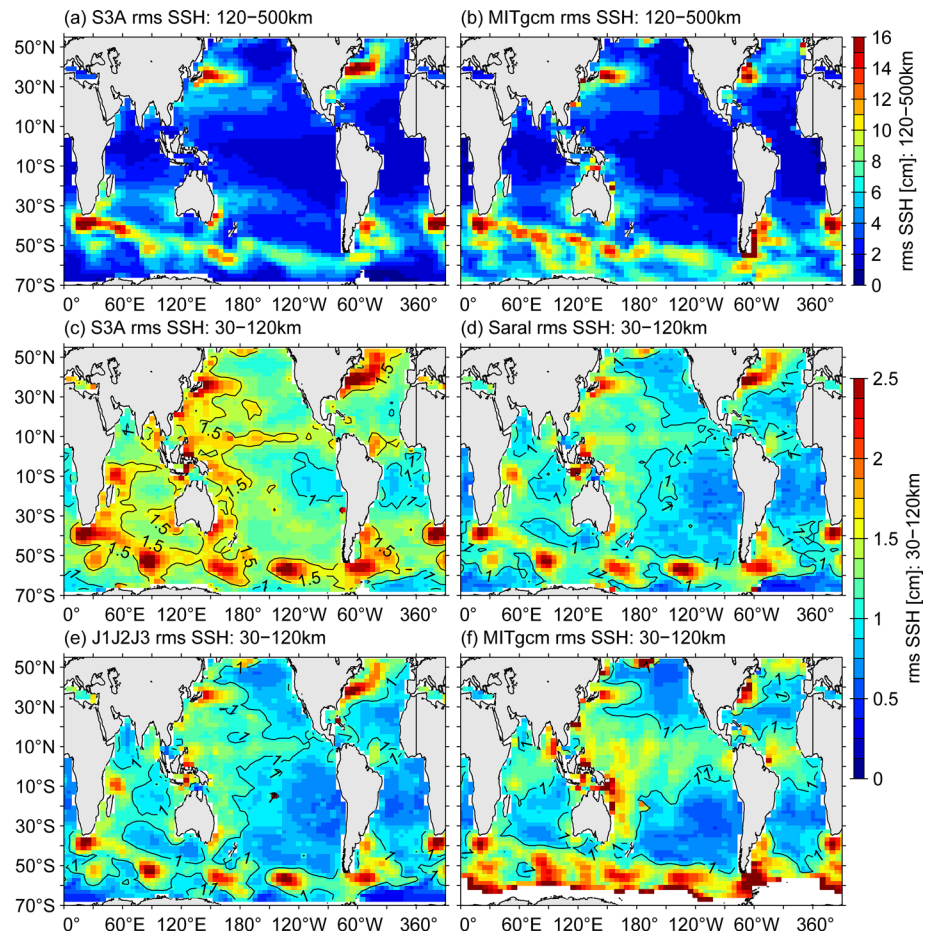


**Figure 3.** Global rms SSH maps in the 120–500 km and 30–120 km wavelength bands for S3A, Saral, J123, and MITgcm: (a) S3A, 120–500 km; (b) MITgcm, 120–500 km; (c) S3A, 30–120 km; (d) Saral, 30–120 km; (e) J123, 30–120 km; and (f) MITgcm, 30–120 km. The rms SSH values along 160°W in panels (a–b) and (c–f) are also displayed in Figures 2a and 2b, respectively. In panel c, contours 1 and 1.5 cm are added, and in panels (d–f), contours 1 cm are added.

a local maximum in the middle of the Pacific tropical basin. The patterns are more consistent among S3A, Saral, and J123 than with MITgcm.

### 3.2. Seasonal Variations of the rms SSH Values in the 30–120 km Wavelength Band

To explore their seasonal variations, the rms SSH values in the 30–120 km wavelength band are first binned for each calendar month and a harmonic analysis with an annual period is then performed separately for S3A, Saral, J123, and MITgcm. Figures 6a–6h show the global distributions of seasonal amplitudes and phases, respectively. Large seasonal amplitudes are seen in west of Australia and in the regions of Kuroshio Extension, Gulf Stream, East Australian Current Extension, and ACC. They are also seen in the northeast Pacific in S3A, Saral, and J123, but less prominently in MITgcm. The global average percentages of the seasonal amplitudes to corresponding yearly mean rms SSH values are 9.1%, 7.6%, 7.4%, and 7.8% for S3A, Saral, J123, and MITgcm, respectively.

North of 15°N and south of 15°S the rms SSH values in the 30–120 km wavelength band reach their maxima in local winter months, i.e., December–February in the northern hemisphere and July–September in the southern hemisphere, when prevailing mid-latitude storms transfer significant amount of wind energy into the upper ocean via near-inertial internal gravity waves (Alford et al., 2016). The wintertime mixed-layer instability can be another contributing factor that enhances the rms SSH variability in the 30–120 km

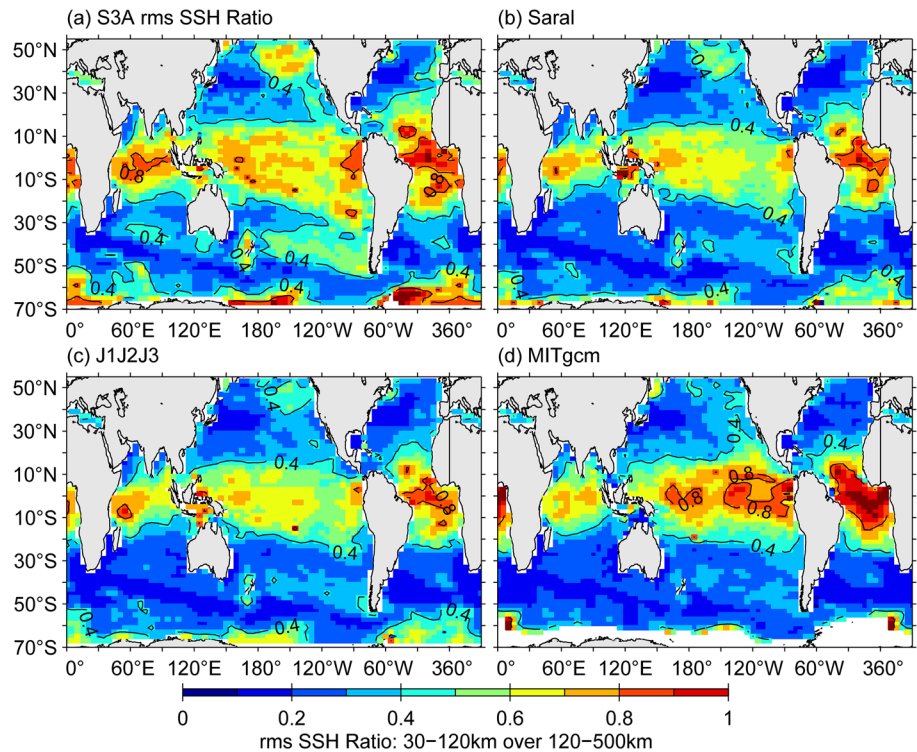


**Figure 4.** Ratios of the rms SSH values in the 30–120 km wavelength band over those in the 120–500 km wavelength band. (a) S3A; (b) Saral; (c) J1J2J3; and (d) MITgcm. Contours 0.4 and 0.8 are added in all panels.

wavelength band (e.g., Mensa et al., 2013; Qiu et al., 2014; Sasaki et al., 2014). Large seasonal amplitudes in the intratropics appear to be linked to the ITCZs and the North and South Equatorial Countercurrents, and their seasonal maxima are reached in local later summer months, i.e., September–November in the northern hemisphere and February–April in the southern hemisphere (Figures 6e–6h), when the North

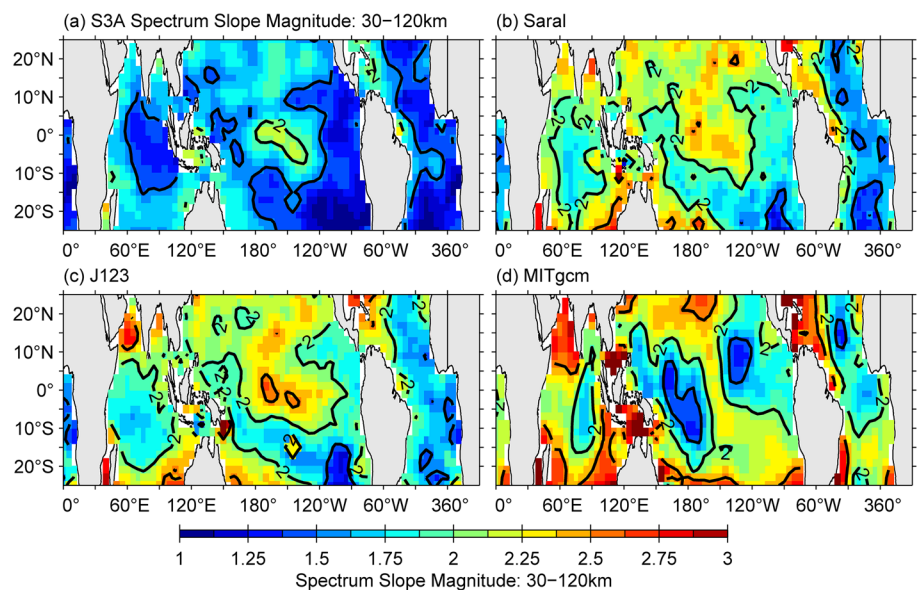


**Figure 5.** Along-track sea surface height (SSH) spectral slope magnitudes in the 30–120 km wavelength band. The spectra always have negative slopes like those at (160°W, 10°S/10°N/25°N) that are shown in Figures 1c–1e. The slope magnitudes are positive. (a) S3A; (b) Saral; (c) J1J2J3; and (d) MITgcm. Contours 1.5, 2, and 2.5 are added in all panels.

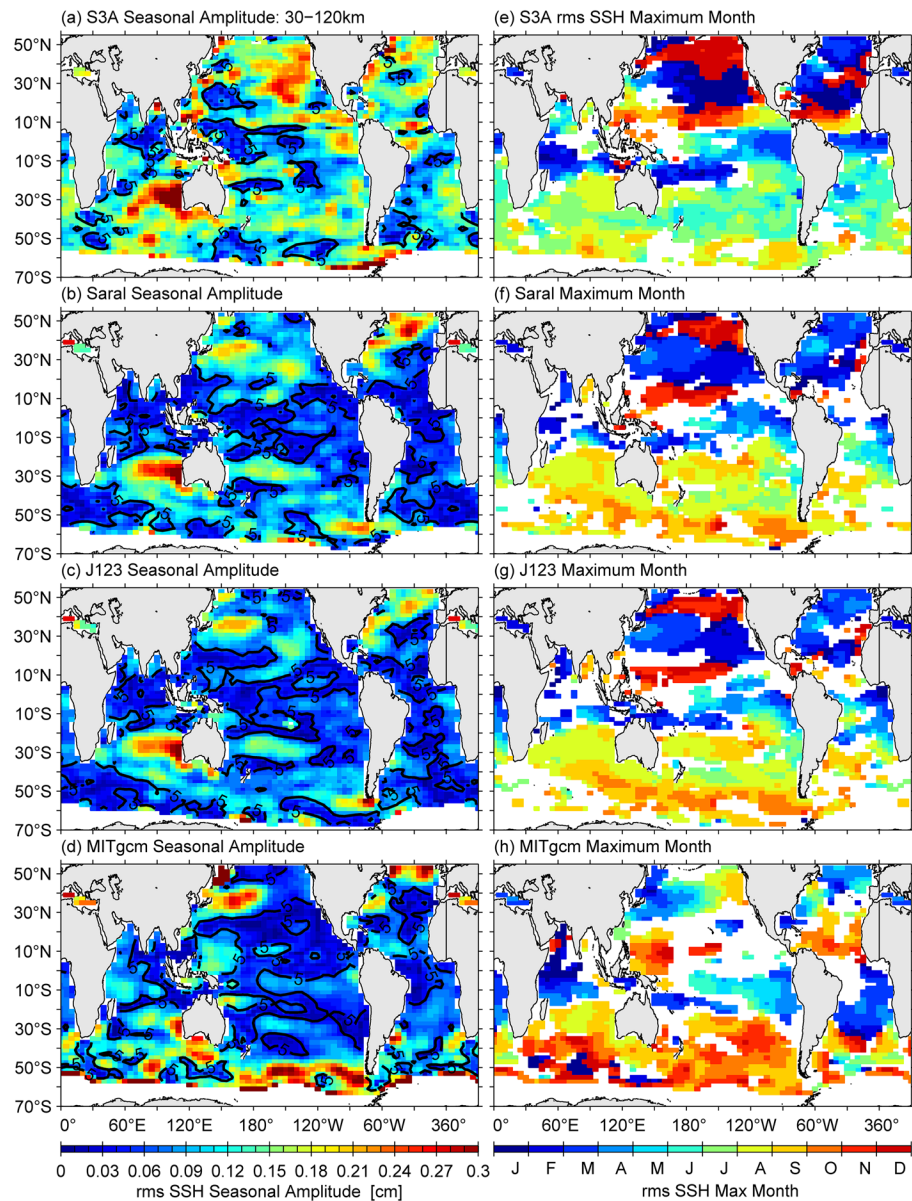


**Figure 6.** Seasonal variations of the rms sea surface height (SSH) values in the 30–120 km wavelength band from the harmonic analyses with an annual period. The left column (panels a–d) is of the amplitudes and the right column of the months when the seasonal variations reach their maxima. The months in the right column are displayed only when their seasonal amplitudes are more than 5% of corresponding yearly mean rms SSH values (5% is contoured in the left column). Panels (a and e) for S3A; (b and f) for Saral; (c and g) for J123; and (d and h) for MITgcm.

and South Equatorial Countercurrents are the strongest (Chen & Qiu, 2004; Godfrey et al., 2001; Hsin & Qiu, 2012).

One noticeable discrepancy between Figures 6h and Figures. 6e–6g is that the seasonal maxima north of 15°N and south of 15°S in MITgcm tend to approach local summer months, i.e., May and June in the northern hemisphere and October and November in the southern hemisphere, instead of local winter months in altimetry missions. Strong summer intensification in 155°E–175°E and 25°N–40°N was identified from the same MITgcm output, mostly in the wavelengths shorter than 25 km (Figure 4c in Rocha, Gille, et al., 2016). Since the MITgcm SSH is regridded into the 1 Hz S3A nominal along-track grid of 6.7 km, this summer intensification is only partially captured in Figure 6h. Meanwhile the summer intensification is absent in Figures 6e–6g.



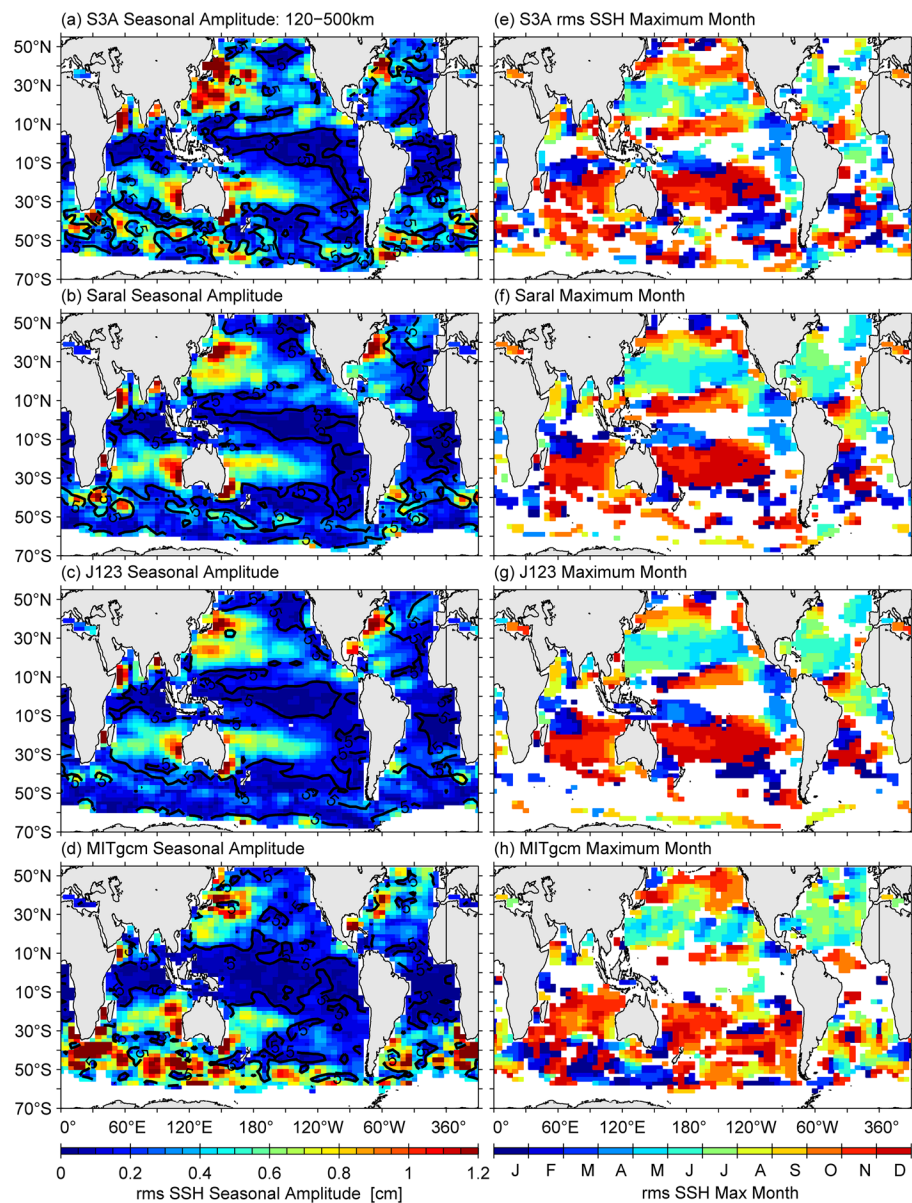


**Figure 7.** Same as Figure 6, except in the 120–250 km wavelength band.

### 3.3. Seasonal Variations of the rms SSH Values in the 120–500 km Wavelength Band

The annual harmonic analysis is also applied to the rms SSH values in the 120–500 km wavelength band (Figures 7a–7h). Large seasonal amplitudes in the 120–500 km wavelength band are seen west of Australia and in the regions of Kuroshio Extension, Gulf Stream, East Australian Current Extension, and ACC where large seasonal amplitudes in the 30–120 km wavelength band were found (Figures 6a–6d). Like the comparisons for the mean rms SSH values (Figures 3a–3f), this similarity is because the same balanced instability dynamics governs the seasonal variations in both the 120–500 km and 30–120 km wavelength bands. Additional large seasonal amplitudes are seen in the regions of the North Pacific STCC ( $\sim 20^{\circ}\text{N}$ – $25^{\circ}\text{N}$ ) and the South Pacific and Indian STCCs ( $\sim 20^{\circ}\text{S}$ – $25^{\circ}\text{S}$ ). As shown in Figures 7e–7h, seasonal variations in the STCC regions reach their maxima in local later spring months, i.e., April–June in the northern hemisphere and October–December in the southern hemisphere, when mesoscale eddies fully evolve to their strongest from baroclinic instability of the vertically sheared background mean currents (Jia et al., 2011; Qiu, 1999; Qiu &

Chen, 2004). The phase patterns associated with the STCCs are not limited to the core regions of the STCCs but extend across the ocean basins.

In Figures 7a–7d, the global average percentages of the seasonal amplitudes to corresponding yearly mean rms SSH values are close to those in the 30–120 km wavelength band: 8.0%, 7.3%, 7.1%, and 8.0% for S3A, Saral, J123, and MITgcm, respectively. In the regions of the ITCZs and the North and South Equatorial Countercurrents, similar local maxima and phase patterns to those in the 30–120 km wavelength band (Figures 6a–6h) are found. This is consistent with the findings from MITgcm by Qiu et al. (2018) that the transition scales from balanced to unbalanced motions can be larger than 250 km within the  $\sim 10^\circ$  latitude from the equator. The large transition scales imply that the unbalanced motions dominate the seasonal variabilities in both 30–120 km and 120–500 km wavelength bands within the  $\sim 10^\circ$  latitude from the equator.

In summary, within  $\sim 10^\circ$  latitude of the equator where the ITCZs and the North and South Equatorial Countercurrents are located, the seasonal rms SSH values in both 30–120 km and 120–250 km wavelength bands reach maxima similarly in local later summer months. Outside this region, the seasonal maximum timing is different: the seasonal rms SSH values in the 30–120 km wavelength band are in local winter months and those in the 120–250 km wavelength band in local later spring months.

#### 4. Summary and Discussion

Global rms SSH values in the 30–120 km wavelength band are estimated by using the along-track SSH measurements from Jason 1/2/3 (J123), Saral/AltiKa (Saral), and Sentinel-3A (S3A, 2 years of LR-RMC data) missions. Despite different measurement error characteristics among the altimetry missions, we find the following consistent results among all altimetry missions and the high-resolution MITgcm simulation.

- High SSH variability in the 30–120 km wavelength band is detected in the intratropics of all ocean basins ( $25^\circ\text{S}$ – $25^\circ\text{N}$ ). Local maxima in the intratropics are linked to the variability by the ITCZs and the North and South Equatorial Countercurrents
- Five regions along the ACC: Agulhas Retroflexion zone, Kerguelen Plateau, Macquarie Ridge, Pacific Antarctic Ridge, and Drake Passage, exhibit significant high SSH variability in the 30–120 km wavelength band
- The average spectral SSH slope in the 30–120 km wavelength band in the intratropics ranges from  $-2.14$  to  $-1.56$ , consistent with the GM model prediction

The global averages of the rms SSH values in the 30–120 km wavelength band from S3A, Saral, and J123 are 1.4, 1.1, and 1.0 cm, respectively. The latter two are 77% and 73% of the first. Despite these amplitude differences, the results from the three altimetry missions share the common geographical patterns. The difference among the missions could be used to indicate the quantitative uncertainties of three samplings of the same field. Because Saral and J123 have high noise floors owing to the spectral humps (Dibarboure et al., 2014) and because the duration of the S3A LR-RMC data is limited to two years, updates from the high-resolution SWOT mission with lower expected noise levels and from longer record of the S3A LR-RMC data with additional data from Sentinel-3B mission are desirable.

Enhanced SSH variability in the 30–120 km wavelength band exists in the intratropics of all ocean basins and in the regions with strong currents like ACC and WBC extensions. Based on the MITgcm simulation analyses (Qiu et al., 2018; Torres et al., 2018), the variability in the intratropics is likely dominated by the unbalanced wave motions while the variability in the strong current regions by the balanced geostrophic motions. Future studies with a focus on the different dynamic processes in the 30–120 km wavelength band are called for.

The MITgcm results are consistently closer to the results from Saral and J123 than from S3A. We speculate that Saral, J123, and MITgcm have resolved similar spatial scales while S3A has resolved finer-scale SSH features. If we assume that the partially resolved scales by altimetry missions are where the SSH spectra exceed the noise floors (Figures 1a–1f), they would be  $\sim 25$  km for Saral and J123 and  $\sim 10$  km for S3A; the resolved scale by MITgcm could be assumed to be  $\sim 23$  km, 10 times the model grid size. As a result, the rms SSH variability in the 30–120 km wavelength band from the wide-swath SWOT mission and from future

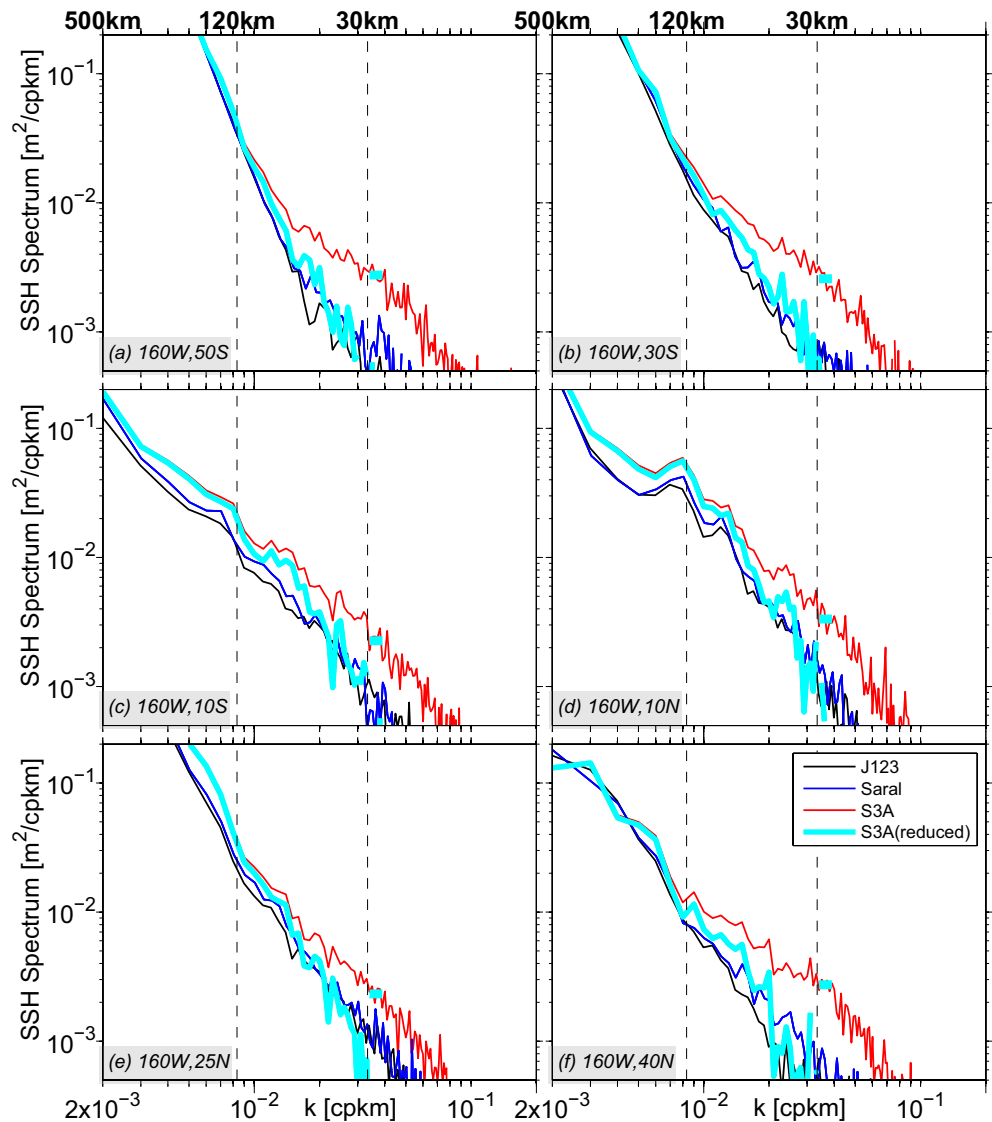


**Figure 8.** The black, blue, and red lines are the same as those in Figures 1a–1f, representing the sea surface height (SSH) spectra after subtracting the noise floors for J123, Saral, and S3A, respectively. The cyan line for S3A (reduced) is derived from the red line for S3A by subtracting its arithmetic average in the 25–30 km wavelength band indicated as a cyan tick on the red line.

higher-resolution model simulations should look like those from S3A: larger rms SSH variability globally and shallower spectral slopes in the intratropics.

An assessment to support these notions is illustrated in Figures 8a–8f: the cyan line for S3A (reduced) is derived from the red line for S3A by subtracting its arithmetic average over the 25–30 km wavelength band. The rms SSH values in the 30–120 km wavelength band associated with the cyan lines are added to Figure 2b, from which we could see that the rms SSH values from the S3A (reduced) approach closer to those from J123 and Saral. From Figures 8a–8f, we notice that removal of the noise floors from the J123 and Saral spectra greatly reduces the variance at the wavelengths shorter than 30 km and that subtracting the arithmetic averages over the 25–30 km wavelength band from the S3A spectra has a similar effect. As such, the difference between the red and cyan lines in Figure 2b suggests that the higher rms SSH values for S3A (red line) are likely because the S3A mission has resolved the variability at the wavelengths shorter than 30 km and has the noise floors that are much lower than the spectral levels in the 30–120 km wavelength band. In this context, the de-noised J123 and Saral data may have underestimated the rms SSH variability in the

30–120 km wavelength band by about 25%. Recall that the global average rms SSH values for Saral and J123 are 77% and 73% of that of S3A, respectively. It will be important for future studies, such as that planned at the SWOT's calibration and validation (CalVal) site off the California coast (Wang et al., 2018), to ascertain this difference and cause behind the different nadir altimetry missions.

## Data Availability Statement

Along-track sea level anomaly L2P products (v3.0) of Jason 1/2/3 and Saral/AltiKa missions in Non-Time-Critical delay were produced and distributed by AVISO+ (<https://www.aviso.altimetry.fr/>), as part of the Ssalto ground processing segment. The two-year time series of Sentinel-3A LR-RMC data (20 Hz along-track sea level anomaly, v2.1) was produced in the framework of the PEACHI project funded by CNES/CLS, and distributed by AVISO+.

## Acknowledgments

The authors thank two anonymous reviewers for their comments that helped improve an early version of the manuscript. The two-year time series of Sentinel-3A LR-RMC data (20 Hz along-track sea level anomaly, v2.1) was produced in the framework of the PEACHI project funded by CNES/CLS, and distributed by AVISO+. This study was supported by NASA OSTST project NN17AH33G.

## References

- Alford, M. H., MacKinnon, J. A., Simmons, H. L., & Nash, J. D. (2016). Near-inertial internal gravity waves in the ocean. *Annual Review of Marine Science*, 8(8), 95–123. <https://doi.org/10.1146/annurev-marine-010814-015746>
- Arbic, B. K., Alford, M. H., Ansong, J. K., Buijsman, M. C., Ciotti, R. B., Farrar, J. T., et al. (2018). A primer on global internal tide and internal gravity wave continuum modeling in HYCOM and MITgcm. In E. Chassignet, A. Pascual, J. Tintornd, & J. Verron (Eds.), *New Frontiers in operational oceanography* (pp. 307–392). <https://doi.org/10.17125/gov2018.ch13>
- Ballarotta, M., Ubelmann, C., Pujol, M.-I., Taburet, G., Fournier, F., Legeais, J.-F., et al. (2019). On the resolutions of ocean altimetry maps. *Ocean Science*, 15, 1091–1109. <https://doi.org/10.5194/os-15-1091-2019>
- Boy, F., Moreau, T., Thibaut, P., Rieu, P., Aublanc, J., Picot, N., et al. (2017). *New stacking method for removing the SAR sensitivity to swell*. Miami, Florida, USA. OSTST Meeting 2017. Oct. 23–27, 2017a.
- Callies, J., & Ferrari, R. (2013). Interpreting energy and tracer spectra of upper-ocean turbulence in the submesoscale range (1–200 km). *Journal of Physical Oceanography*, 43, 2456–2474. <https://doi.org/10.1175/jpo-d-13-063.1>
- Chelton, D. B., Schlax, M. G., & Samelson, R. M. (2011). Global observations of nonlinear mesoscale eddies. *Progress in Oceanography*, 91, 167–216. <https://doi.org/10.1016/j.pocean.2011.01.002>
- Chen, S., & Qiu, B. (2004). Seasonal variability of the South Equatorial Countercurrent. *Journal of Geophysical Research*, 109, C08003. <https://doi.org/10.1029/2003JC002243>
- Chereskin, T., Rocha, C., Gille, S., Menemenlis, D., & Passaro, M. (2019). Characterizing the transition from balanced to unbalanced motions in the southern California Current. *Journal of Geophysical Research: Oceans*, 124, 2088–2109. <https://doi.org/10.1029/2018jc014583>
- Dibarboure, G., Boy, F., Desjonqueres, J. D., Labroue, S., Lasne, Y., Picot, N., et al. (2014). Investigating short-wavelength correlated errors on low-resolution mode altimetry. *Journal of Atmospheric and Oceanic Technology*, 31(6), 1337–1362. <https://doi.org/10.1175/jtech-d-13-00081.1>
- Ducet, N., Le Traon, P. Y., & Reverdin, G. (2000). Global high-resolution mapping of ocean circulation from TOPEX/Poseidon and ERS-1 and -2. *Journal of Geophysical Research*, 105, 19477–19498. <https://doi.org/10.1029/2000jc900063>
- Dufau, C., Orszynowicz, M., Dibarboure, G., Morrow, R., & Le Traon, P. Y. (2016). Mesoscale resolution capability of altimetry: Present and future. *Journal of Geophysical Research: Oceans*, 121, 4910–4927. <https://doi.org/10.1002/2015jc010904>
- Fu, L.-L., Lee, T., Liu, W., & Kwok, R. (2019). 50 years of satellite remote sensing of the ocean. In *A century of progress in atmospheric and related sciences*. American Meteorological Society, 59(1). <https://doi.org/10.1175/amsmonographs-d-18-0010.1>
- Godfrey, J., Johnson, G., McPhaden, M., Reverdin, G., & Wijffels, S. (2001). The tropical ocean circulation. In G. Siedler, J. Church, & J. Gould (Eds.), *Ocean circulation and climate: Observing and modelling the global ocean* (pp. 215–246). Elsevier.
- Hsin, Y.-C., & Qiu, B. (2012). Seasonal fluctuations of the surface North Equatorial Countercurrent (NECC) across the Pacific basin. *Journal of Geophysical Research*, 117, C06001. <https://doi.org/10.1029/2011JC007794>
- Jia, F., Wu, L., & Qiu, B. (2011). Seasonal modulation of eddy kinetic energy and its formation mechanism in the southeast Indian Ocean. *Journal of Physical Oceanography*, 41, 657–665. <https://doi.org/10.1175/2010jpo4436.1>
- Marshall, J., Adcroft, A., Hill, C., Perelman, L., & Heisey, C. (1997). A finite-volume, incompressible navier stokes model for studies of the ocean on parallel computers. *Journal of Geophysical Research*, 102, 5753–5766. <https://doi.org/10.1029/96jc02775>
- Menemenlis, D., Campin, J.-M., Heimbach, P., Hill, C. C., Nguyen, A., Schodlok, M., et al. (2008). ECCO2: High-resolution global ocean and sea ice data synthesis. *Mercator Ocean Quarterly Newsletter*, 31, 13–21.
- Mensa, J. A., Garraffo, Z., Griffa, A., Özgökmen, T. M., Haza, A., & Veneziani, M. (2013). Seasonality of the submesoscale dynamics in the Gulf Stream region. *Ocean Dynamics*, 63, 923–941. <https://doi.org/10.1007/s10236-013-0633-1>
- Moreau, T., Cadier, E., Boy, F., Aublanc, J., Rieu, P., Raynal, M., et al. (2021). High-performance altimeter Doppler processing for measuring sea level height under varying sea state conditions. *Advances in Space Research*, 67, 1870–1886. <https://doi.org/10.1016/j.asr.2020.12.038>
- Morrow, R., Blumstein, D., & Dibarboure, G. (2018). Fine-scale altimetry and the future SWOT mission. In E. Chassignet, A. Pascual, J. Tintornd, & J. Verron (Eds.), *New frontiers in operational oceanography* (pp. 191–226). <https://doi.org/10.17125/gov2018.ch08>
- Morrow, R., Fu, L.-L., Arduin, F., Benkiran, M., Chapron, B., Cosme, E., et al. (2019). Global observations of fine-scale ocean surface topography with the surface water and ocean topography (SWOT) mission. *Frontiers in Marine Science*, 6, 232. <https://doi.org/10.3389/fmars.2019.00232>
- Munk, W. (1981). Internal Waves and Small-Scale Processes. In B. A. Warren, & C. Wunsch (Eds.), *Evolution of physical oceanography* (pp. 264–291). MIT OpenCourseWare.
- Qiu, B. (1999). Seasonal eddy field modulation of the North Pacific Subtropical Countercurrent: TOPEX/POSEIDON observations and theory. *Journal of Physical Oceanography*, 29, 2471–2486. [https://doi.org/10.1175/1520-0485\(1999\)029<2471:sefmot>2.0.co;2](https://doi.org/10.1175/1520-0485(1999)029<2471:sefmot>2.0.co;2)
- Qiu, B., & Chen, S. (2004). Seasonal modulations in the eddy field of the South Pacific Ocean. *Journal of Physical Oceanography*, 34, 1515–1527. [https://doi.org/10.1175/1520-0485\(2004\)034<1515:smitef>2.0.co;2](https://doi.org/10.1175/1520-0485(2004)034<1515:smitef>2.0.co;2)



- Qiu, B., Chen, S., Klein, P., Sasaki, H., & Sasai, Y. (2014). Seasonal mesoscale and submesoscale eddy variability along the North Pacific Subtropical Countercurrent. *Journal of Physical Oceanography*, *44*, 3079–3098. <https://doi.org/10.1175/jpo-d-14-0071.1>
- Qiu, B., Chen, S., Klein, P., Wang, J., Torres, H., Fu, L.-L., & Menemenlis, D. (2018). Seasonality in transition scale from balanced to unbalanced motions in the world ocean. *Journal of Physical Oceanography*, *48*, 591–605. <https://doi.org/10.1175/jpo-d-17-0169.1>
- Qiu, B., Nakano, T., Chen, S., & Klein, P. (2017). Submesoscale transition from geostrophic flows to internal waves in the northwestern Pacific upper ocean. *Nature Communications*, *8*, 14055. <https://doi.org/10.1038/ncomms14055>
- Rocha, C., Gille, S., Chereskin, T., & Menemenlis, D. (2016). Seasonality of submesoscale dynamics in the Kuroshio extension. *Geophysical Research Letters*, *43*, 11304–11311. <https://doi.org/10.1002/2016GL071349>
- Rocha, C. B., Chereskin, T. K., Gille, S. T., & Menemenlis, D. (2016). Mesoscale to submesoscale wavenumber spectra in Drake Passage. *Journal of Physical Oceanography*, *46*, 601–620. <https://doi.org/10.1175/jpo-d-15-0087.1>
- Sasaki, H., Klein, P., Qiu, B., & Sasai, Y. (2014). Impact of oceanic-scale interactions on the seasonal modulation of ocean dynamics by the atmosphere. *Nature Communications*, *5*, 5636. <https://doi.org/10.1038/ncomms6636>
- Torres, H., Klein, P., Menemenlis, D., Qiu, B., Su, Z., Wang, J., et al. (2018). Partitioning ocean motions into balanced motions and internal gravity waves: A modeling study in anticipation of future space missions. *Journal of Geophysical Research: Oceans*, *123*, 8084–8105. <https://doi.org/10.1029/2018jc014438>
- Vergara, O., Morrow, R., Pujol, I., Dibarboure, G., & Ubelmann, C. (2019). Revised global wave number spectra from recent altimeter observations. *Journal of Geophysical Research: Oceans*, *124*, 3523–3537. <https://doi.org/10.1029/2018jc014844>
- Wang, J., Fu, L.-L., Qiu, B., Menemenlis, D., Farrar, J. T., Chao, Y., et al. (2018). An observing system simulation experiment for the calibration and validation of the surface water ocean topography sea surface height measurement using in situ platforms. *Journal of Atmospheric and Oceanic Technology*, *35*, 281–297. <https://doi.org/10.1175/jtech-d-17-0076.1>
- Wang, J., Fu, L.-L., Torres, H. S., Chen, S., Qiu, B., & Menemenlis, D. (2019). On the spatial scales to be resolved by the surface water and ocean topography Ka-band radar interferometer. *Journal of Atmospheric and Oceanic Technology*, *36*, 87–99. <https://doi.org/10.1175/jtech-d-18-0119.1>
- Xu, Y., & Fu, L.-L. (2012). The effects of altimeter instrument noise on the estimation of the wavenumber spectrum of sea surface height. *Journal of Physical Oceanography*, *42*, 2229–2233. <https://doi.org/10.1175/JPO-D-12-0106.1>